# REPORT DOCUMENTATION PAGE

| 1. REPORT DATE *(DD-MM-YYYY)* | 2. REPORT TYPE | 3. DATES COVERED *(From - To)* |
|---|---|---|
| 7/31/2012 | Final report | 5/1/2009-4/30/2012 |

| 4. TITLE AND SUBTITLE | 5a. CONTRACT NUMBER |
|---|---|
| HIGH PERFORMANCE ORGANIC SEMICONDUCTORS | |
| | **5b. GRANT NUMBER** <br> FA9550-09-1-0256 |
| | **5c. PROGRAM ELEMENT NUMBER** |

| 6. AUTHOR(S) | 5d. PROJECT NUMBER |
|---|---|
| Zhenan Bao | |
| | **5e. TASK NUMBER** |
| | **5f. WORK UNIT NUMBER** |

| 7. PERFORMING ORGANIZATION NAME(S) AND ADDRESS(ES) | 8. PERFORMING ORGANIZATION REPORT NUMBER |
|---|---|
| Stanford University <br> 381 North South Mall <br> Stanford, CA 94305 | |

| 9. SPONSORING / MONITORING AGENCY NAME(S) AND ADDRESS(ES) | 10. SPONSOR/MONITOR'S ACRONYM(S) |
|---|---|
| AFOSR <br> 875 N Randolph St <br> Arlington, VA  22203 | |
| | **11. SPONSOR/MONITOR'S REPORT NUMBER(S)** <br> AFRL-OSR-VA-TR-2012-0976 |

**12. DISTRIBUTION / AVAILABILITY STATEMENT**

Distribution A: Approved for Public Release

**13. SUPPLEMENTARY NOTES**

**14. ABSTRACT**
This report summarizes results supported by grant no. FA9550-09-1-0256. We report: 1. Development of new n-type dopants 2. Synthesis of semiconducting polymers based on acenes; 3. Tuning threshold voltage of organic transistors with self assembled monolayers; 4. A new method to achieve high mobility aligned single crystals over a large area; 5. The electronic skin concept.

**15. SUBJECT TERMS**

| 16. SECURITY CLASSIFICATION OF: | | | 17. LIMITATION OF ABSTRACT | 18. NUMBER OF PAGES | 19a. NAME OF RESPONSIBLE PERSON <br> Dr. Charles Lee |
|---|---|---|---|---|---|
| **a. REPORT** | **b. ABSTRACT** | **c. THIS PAGE** | U | 26 | **19b. TELEPHONE NUMBER** *(include area code)* <br> 703-696-7779 |
| U | U | U | | | |

# Final Report
# FA9550-09-1-0256
# Zhenan Bao

**1.      Development of DMBI iodide salts as the n-type dopant precursors by vacuum deposition**

Controllable molecular doping of organic semiconductors has important advantages for organic light-emitting diodes (OLEDs), organic solar cells (OSCs)  and organic thin-film transistors (OTFTs). Previous studies on doping of organic semiconductors showed that the addition of strong electron donors or acceptors as dopants can generate extra electrons or holes, respectively. This leads to a shift in Fermi level and improves film conductivity. Furthermore, an Ohmic contact can be formed by a highly doped layer at the interface between the metal electrode and the organic semiconductor layer such that good charge injection or extraction can be achieved in spite of energy barriers between the electrode and organic semiconductor layer. For example, efficient doping in organic transporting layers resulted in very low operational voltages of OLEDs with a high power efficiency of 90 lm/W. Doping also enabled the fabrication of tandem structures for efficient OSCs using a versatile organic recombination contact.  Additionally, our group has recently reported that intentional n-type doping can improve air-stability of n-channel OTFTs.

A number of molecular p-type dopants have been investigated, such as $F_4$-TCNQ and $C_{60}F_{36}$. Recently, n-type molecular doping has drawn interests to replace the reactive alkali metals as dopants to prevent high diffusivity and difficulty in handling. However, efficient n-type molecular doping is challenging since the dopant's highest occupied molecular orbital (HOMO) level must be above the lowest unoccupied molecular orbital (LUMO) level of the organic semiconductor matrix, in order to make the electron transfer process favorable. The required HOMO of the dopant is usually so shallow that it is unstable in air, complicating their fabrication process and limiting their applications in organic electronics. One approach is using new dopants with shallow HOMOs, which are still stable in air, such as tetrathianaphthacene (TTN). But they are not strong enough donors to obtain high n-type doped film conductivity. Another approach is to use stable cationic salt precursors, such as pyronin B (PyB) chloride, triphenylmethane cationic dyes crystal violet (CV) and acridine orange base [3,6-bis(dimethylamino)acridine (AOB)], to *in situ* generate the volatile electron donors upon heating for n-type doping. Recently, a series of air-stable dimers of sandwich compounds, including rhodocene and (pentamethylcyclopentadienyl)(arene)ruthenium and iron derivatives, were reported as highly reducing n-type dopants for a variety of electron transport materials processed by either vacuum or solution, with electron affinities as small as 2.8 eV. In this approach, a thermodynamically unfavorable reversible cleavage of the dimers occurs followed by a rapid irreversible electron transfer from the highly reactive monomer radical. Compared to the precursor approach (e.g. PyB), chemical side reactions are minimized and electron transporting materials with high LUMOs can be doped n-type by these dimers. Although several air-stable molecular n-type dopants have been reported, the highest reported conductivity of the n-type doped organic film with air-stable molecular dopants is still low, only ca. $4.9 \times 10^{-2}$ S/cm with $C_{60}$ as the matrix. Therefore, it remains challenging to develop air-stable molecular n-type dopants, coupled with strong doping ability, to achieve high film conductivities for applications in organic electronic devices.

Recently, our group introduced (4-(1,3-dimethyl-2,3-dihydro-1*H*-benzoimidazol-2-yl)phenyl)dimethylamine (N-DMBI) as a solution processable dopant with efficient n-type doping ability, and the conductivity of the doped  [6,6]-phenyl $C_{61}$ butyric acid methyl ester (PCBM) film was significantly increased. In this communication, we demonstrate the use of its cationic derivative, 2-(2-methoxyphenyl)-1,3-dimethyl-1*H*-benzoimidazol-3-ium iodide (o-MeO-DMBI-I, Figure 1), as an n-type dopant for vacuum processed n-channel semiconductors. Film conductivity as high as 5.5 S/cm was obtained.
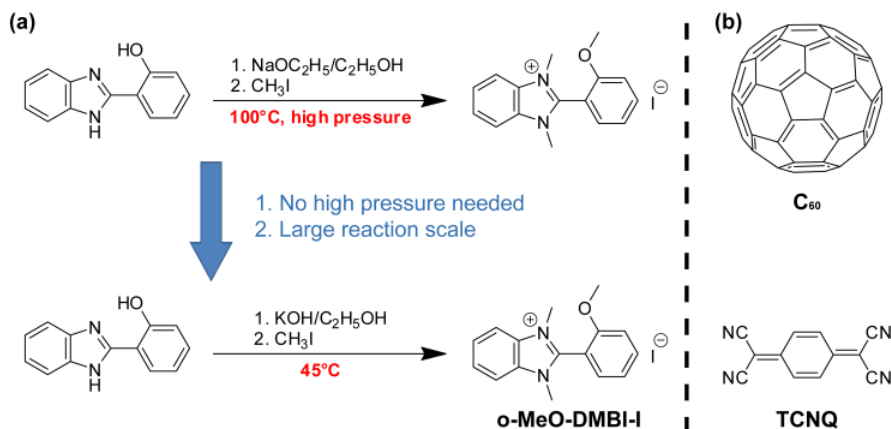
**Figure 1**. (a) Chemical structure of o-MeO-DMBI-I and its modified synthetic route. (b) Chemical structures of n-channel semiconductors: $C_{60}$ and TCNQ.

There was only one previous paper reporting the synthesis of o-MeO-DMBI-I via a two-step reaction from 1,2-diaminobenzene and 2-methoxybenzoic acid, in which o-MeO-DMBI-I was the side product. In our work, we modified the reported synthetic route of 1,3-dimethyl-2-phenyl-1$H$-benzoimidazol-3-ium iodide (DMBI-I), by using a large excess of methyl iodide (MeI) such that the high pressure reaction condition previously reported can be eliminated. Our new method can easily produce a large quantity of the target compound. o-MeO-DMBI-I is air-stable, which can be stored and handled in air for extended periods without degradation.

To characterize the n-type doping ability of o-MeO-DMBI-I, the film conductivity of fullerene $C_{60}$, a well-known n-channel semiconductor, was investigated. n-Type doping of $C_{60}$ was previously shown to be essential to fabricate efficient tandem solar cell structures. Effective n-type doping of $C_{60}$ is needed to create low loss contacts between the stacked cells while maintaining a very thin doped $C_{60}$ layer to minimize parasitic absorption losses. In our experiments, $C_{60}$ and o-MeO-DMBI-I were co-deposited from separate sources at high vacuum onto smooth glass substrates to give films of 30 nm in thickness. Different doping concentrations were achieved by accurate control of the deposition rates of the matrix and dopant materials using separate quartz microbalances. The conductivity of o-MeO-DMBI-I doped $C_{60}$ films were measured in high vacuum and the results were shown in Figure 2a. The conductivity of undoped $C_{60}$ film was only $6.6 \times 10^{-8}$ S/cm. Upon doping, the film conductivity significantly increased by more than 7 orders of magnitude. The highest film conductivity of 5.5 S/cm was obtained by 8.0wt% (14mol%) doping. This is the highest reported film conductivity by molecular n-type doping. As a reference, the typical film conductivity of the well-known conducting polymer, poly(3,4-ethylenedioxy-thiophene) poly(styrenesulfonate) (PEDOT:PSS), without solvent additives such as dimethyl sulfoxide (DMSO) or ethylene glycol (EG) is in the range between 0.1~1 S/cm. This indicates the strong n-type doping ability of o-MeO-DMBI-I and makes it promising for applications in organic electronic devices. At higher doping concentration of 12wt% (21mol%), the conductivity decreased a little to 1.8 S/cm, which can be attributed to the tendency of o-MeO-DMBI-I for aggregation and the localization of the donated electrons around dopant molecules in the films.
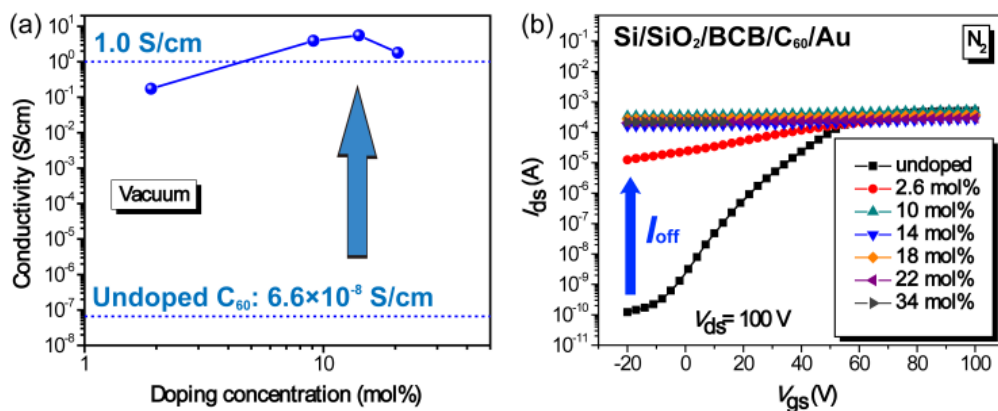


**Figure 2**. (a) The conductivity of undoped and o-MeO-DMBI-I doped $C_{60}$ films at varying doping concentrations. (b) Transfer characteristics of o-MeO-DMBI-I doped $C_{60}$ OTFTs at varying doping concentrations.

To further confirm the n-type doping effect of o-MeO-DMBI-I in $C_{60}$ films, n-channel transistors were fabricated with a bottom-gate, top-contact configuration on n-doped silicon substrates with 300-nm-thick thermally grown $SiO_2$. We passivated the $SiO_2$ surface using a thin (20 nm), thermally crosslinked divinyltetra-methyldisiloxane bis(benzocyclobutene) (BCB) layer to eliminate the electron traps due to the surface hydroxyl groups on $SiO_2$. In a $N_2$-filled glovebox, the undoped $C_{60}$ transistors exhibited a high average electron mobility of $4.02\pm0.35$ cm$^2$/(V·s) and an average on-off ratio of $(4.68\pm1.04)\times10^6$. All the doped transistors showed expected significant decrease of the on-off ratio due to increase of off-current (Figure 2b).[3d,4b] With only 1.4wt% (2.6mol%) o-MeO-DMBI doping, the device already exhibited a low on-off ratio of less than 100. At higher doping concentrations, devices showed little gate field-dependent characteristics with on-off ratios of <10, indicating the films were essentially conductive.

To study the origin of the n-type doping effect of o-MeO-DMBI-I, we carried out UV-Vis-NIR absorption spectra measurement on the doped $C_{60}$ films by vacuum deposition. In our experiments, we could not observe the $C_{60}$ anion peaks at 1000~1200 nm arising from electron transfer, because the $C_{60}$ anion is too unstable in air to be detected due to its high LUMO level. Therefore, to confirm the electron transfer from o-MeO-DMBI-I to the n-channel matrix, we doped 7,7,8,8-tetracyanoquino-dimethane (TCNQ), another well-known n-channel semiconductor, which has a much lower LUMO level (-4.8 eV), with o-MeO-DMBI-I. In this case, the anion peaks can be observed in the absorption spectra even under ambient conditions. We fabricated the o-MeO-DMBI-I doped TCNQ films by vacuum co-deposition at a doping concentration of 35wt% (22mol%). In the absorption spectra, the strong TCNQ anion peaks (764 nm and 865 nm) were observed in air, indicating that efficient electron transfer had occurred from o-MeO-DMBI-I to TCNQ molecules (Figure 3a).
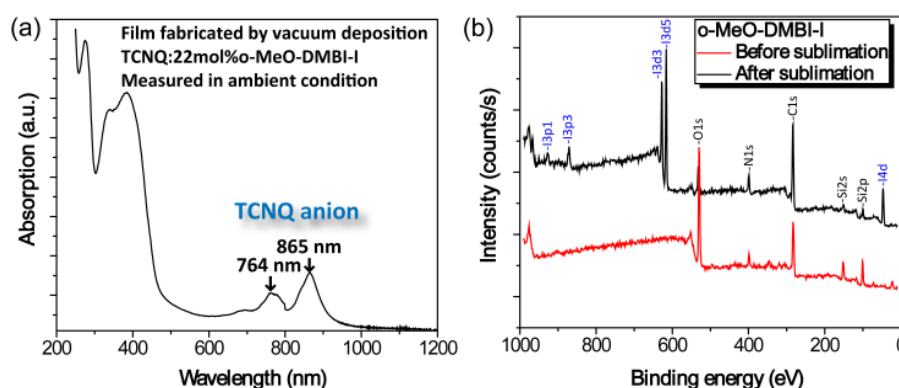


**Figure 3**. (a) The UV-Vis-NIR absorption spectra of 35wt% (22mol%) o-MeO-DMBI-I doped TCNQ film fabricated by vacuum deposition. (b) The X-ray photoelectron spectroscopy (XPS) spectra of o-MeO-DMBI-I before/after sublimation at high vacuum.

In our previous work on solution processable n-type dopant N-DMBI, we speculated that the key species enabling effective n-type doping was its neutral radicals, whose singly occupied molecular orbital (SOMO) level is very high. According to Gaussian 03 calculations (B3LYP/6-31G*), it is at -2.36 eV. Thus, the neutral radicals allowed for electron transfer from the dopant to the n-channel semiconductors. The reported studies on the cationic salts of PyB and CV showed that their protonated leuco base can be generated *in situ* during vacuum deposition, followed by the formation of neutral radicals with a low-ionization-energy state, which is responsible for n-type doping. We hypothesize that o-MeO-DMBI-I was reduced during evaporation at the deposition temperature (180°C~200°C) in high vacuum such as to form the neutral radicals with much higher SOMO level (-2.53 eV by Gaussian 03' calculation). The doping takes place by electron transfer from the neutral radicals to $C_{60}$ molecules and o-MeO-DMBI-I was re-oxidized to the cationic form. Then, the mass spectra were measured *in situ* in the vacuum chamber while evaporating o-MeO-DMBI-I at its deposition temperature (180°C~200°C). The peak at 254.3 amu was clearly observed, which is assigned to 2-(2-methoxyphenyl)-1,3-dimethyl-2,3-dihydro-1*H*-benzoimidazole (o-MeO-DMBI, molecular weight: 254.3), indicating the formation of o-MeO-DMBI during evaporation. To further elucidate the doping mechanism, X-ray photoelectron spectroscopy (XPS) was used to measure pure o-MeO-DMBI-I films fabricated by vacuum deposition and drop casting from ethanol solution, respectively (Figure 3b). By comparison, no iodide peak was observed in the XPS spectra of neat o-MeO-DMBI-I film fabricated by vacuum deposition, indicating o-MeO-DMBI-I was reduced and lost I⁻ during evaporation. And this also demonstrated that the lost I⁻ in this precursor

approach didn't contaminate the doping films. Moreover, we also fabricated o-MeO-DMBI-I doped PCBM films at a doping concentration of 2.0wt% (4.7mol%) by solution spin-coating deposition. The entire process was carried out at below 100$^0$C. In this case, we found no n-type doping effect by both conductivity and transistor measurements. These results indicate that o-MeO-DMBI-I is an n-type dopant precursor, and the doping effect can be only obtained by heating to form the neutral radicals, which is responsible for the strong n-type doping effect. Besides, our preliminary results showed that o-MeO-DMBI-I can also effectively n-type dope the organic semiconductors with LUMO level as high as -3.0 eV. Our further investigation of the n-type doping effect of o-MeO-DMBI-I on different organic semiconductors with higher LUMO (> -3.0 eV) is still in progress to further explore the limit of the n-type doping achievable with o-MeO-DMBI-I.

In summary, we have synthesized a new air-stable n-type dopant, o-MeO-DMBI-I, for vacuum processed organic thin films. C$_{60}$ can be highly doped by o-MeO-DMBI-I, which was shown from measurements of film conductivity and transistors. The highest film conductivity obtained was 5.5 S/cm in this work, indicating it is promising for the application in various organic electronic devices. Systematic studies on the doping mechanisms of o-MeO-DMBI-I and other DMBI-I derivatives are underway as well as their applications in solar cells.

## 2.      Mechanistic investigations of the new n-type dopants.

We performed detailed analysis and mechanistic studies for the solution doped systems with PCBM and N-DMBI. We expect the mechanism for the vacuum evaporated dopant is similar. Compositional analysis of the precipitate from mixing PCBM and N-DBMI was accomplished by DART-TOF-MS and C:H:N elemental analysis. DART-TOF-MS identified PC$_{61}$BM radical anions, but could not unequivocally identify dopant ions in the precipitate. Elemental analysis confirmed the presence of nitrogen in a C:N ratio consistent with a near 1:1 mixture of dopant to PC$_{61}$BM (Calculated: C, 90.63; H, 2.85; N, 2.40 Found: C, 86.24; H, 2.13; N, 1.93 C:N Ratio Calculated: 37.8 C:N Ratio Found: 44.7).
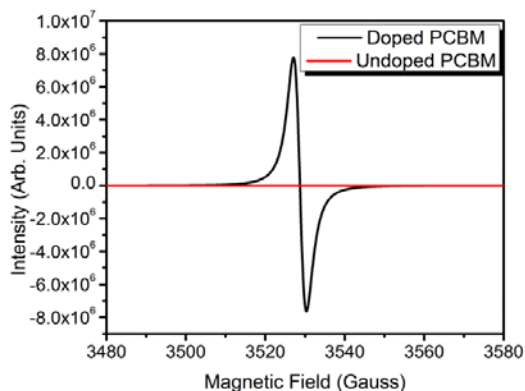


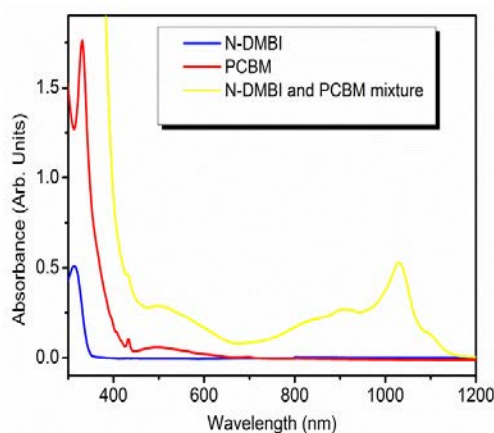**Figure4:** X-band EPR of o-MeO-DMBI doped and undoped PCBM thin films at 298 K.

**Figure 5:** UV-Vis-NIR spectra of N-DMBI, PCBM and N-DMBI/PCBM at 298 K.

X-band EPR of solutions and thin-films gave a radical signal consistent with a $S = 1/2$ PC$_{61}$BM radical anion ($g = 1.998$) (Figure 4). The presence of a PC$_{61}$BM radical anion was further substantiated by the absorption at 1020 nm in the UV-Vis-NIR spectrum of N-DMBI or o-MeO-DMBI and PC$_{61}$BM solutions (Figure 5). A Comparison with literature supports the assignment of the NIR absorption at 1020 nm as the transition from the singly occupied to the nearest unoccupied molecular orbital of a PC$_{61}$BM radical anion. Pure samples of PC$_{61}$BM or DMBI dopants were EPR silent and had no significant absorption in the NIR.

The EPR and UV-Vis-NIR studies established that the product of the doping reaction is likely a fullerene radical anion and dopant charge transfer complex. The kinetics of the reaction were then studied using both UV-Vis-NIR and $^1$H-NMR spectroscopy. The growth of the absorption at 1020 nm was followed at various concentrations of N-DMBI and PC$_{61}$BM. The first-order dependence of the reaction on both N-DMBI and PC$_{61}$BM is clear from the initial rate data. The decay rates of the starting material $^1$H-NMR peaks could also be determined despite the formation of a paramagnetic precipitate. A first-order dependence on PC$_{61}$BM was also found under pseudo first-order conditions (10x o-MeO-DMBI) in the reaction with o-MeO-DMBI as followed by $^1$H-NMR kinetics.

The first order dependence of the reaction on PC$_{61}$BM rules out the possibility that DMBI dopants undergo spontaneous C-H bond homolysis in the annealing step (Mechanism 2, **Scheme 1**). However, several mechanisms can still be envisioned. A strong primary kinetic isotope effect (KIE) would be predicted for mechanisms **3** and **4** (**Scheme 1**); mechanism **1** is expected to exhibit a secondary KIE.
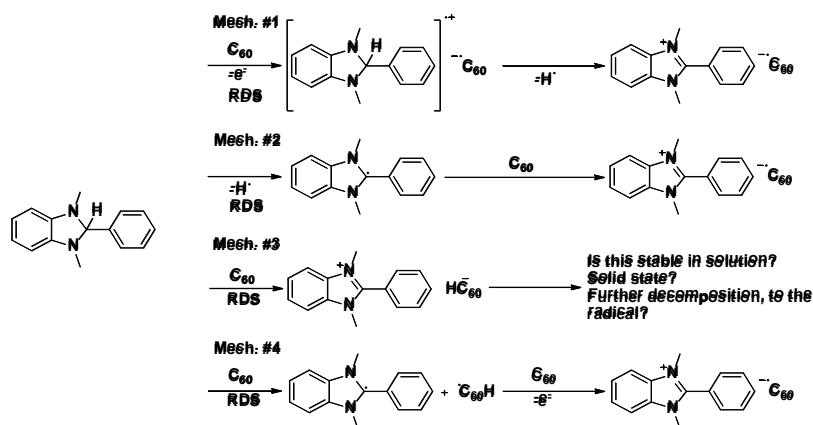
**Scheme 1:** Potential doping mechanisms

An attempted preparation of deutero-N-DMBI (d-N-DMBI) by deuteration of the corresponding imidazolium salt with sodium borodeuteride (NaBD$_4$) resulted in 16% hydride incorporation (Reaction 1, **Scheme 2**). The incorporation of hydrides may have been the consequence of both the low isotopic purity of NaBD$_4$ (98% deuteride) and of a primary KIE in the deuteration reaction. Thus, an alternative synthesis was needed to obtain d-N-DMBI. Preparation of deutero-*para*-dimethylaminobenzaldehyde was accomplished by the Vilsmeier-Haack reaction of DMF-d$_7$ with dimethylaminobenzene (Reaction 2, **Scheme 2**). Condensation with diamine **4** resulted in isotopically pure d-N-DMBI with a deuterium incorporation of ~99.5% as determined by comparison of the hydride peak with select C$_{13}$ satellites (Reaction 3, **Scheme 2**). Electrospray ionization mass spectrometry (ESI-MS) further confirmed the deuteration of this material. A primary KIE of 4 was observed by both UV-Vis-NIR and ${}^1$H-NMR kinetics in the reaction of d-N-DMBI with PC$_{61}$BM. This observation is consistent with either mechanism **3** or **4** (**Scheme 1**).
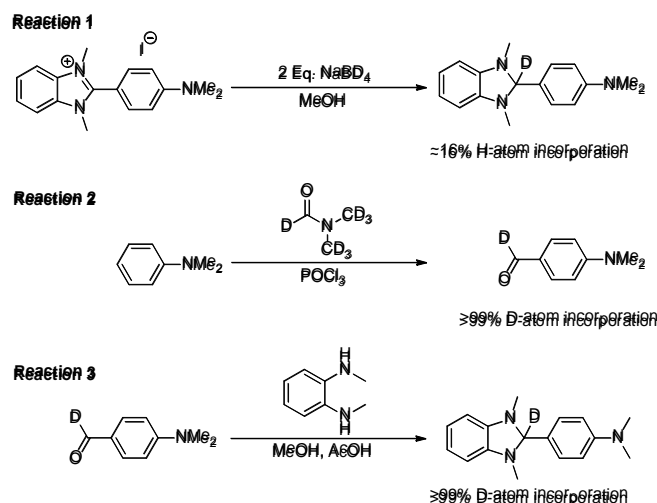


**Scheme 2:** Synthesis of d-N-DMBI

1H-benzimidazoles and benzimidazolium salts have been introduced as practical n-dopants for solution and vacuum deposition respectively. The morphology and conductivity of solution processed 1H-benzimidazole doped PC$_{61}$BM thin-films is dependent upon the mixing time before spin coating. The precipitation of a dopant/PC$_{61}$BM charge transfer complex is responsible for the batch-to-batch morphological and electrical variations. Chemical characterization of the dopant/PC$_{61}$BM charge transfer complex was accomplished by ESI-MS, C:H:N elemental analysis, EPR and UV-Vis-NIR spectroscopy. Comparison of the mass spectra of the doping products of N-DMBI and d-N-DMBI with PC$_{61}$BM will be used to determine the final location of the unaccounted for hydrogen (deuterium) atom. UV-Vis-NIR and ${}^1$H-NMR rate studies revealed a first-order dependence on both the dopant and PC$_{61}$BM for the doping reaction. Moreover, a strong primary KIE effect was revealed. Hammett and solvent polarity studies will be used to distinguish between mechanisms **3** and **4** (**Scheme 1**).

Our current understanding indicates a dependence of the doping rate on the strength of the active C-H bond and on the energy levels of the acceptor. Consequently, the application of 1H-benzimidazole dopants may be limited to materials that are capable of accepting a hydride or that have very low LUMO energies. Future studies will be aimed at understanding the interplay and limitations imposed by different dopant/host combinations. Additionally, new n-dopant precursors with weaker homolyzable bonds or n-dopants that require no activation will be explored.

## 3. New high mobility polymer design and synthesis.

While the molecular engineering of larger linear acenes have resulted in charge transport properties superceding those of amorphous silicon, the incorporation of such moieties in polymers for functional conjugated materials is a relatively underexplored area of study. Previously, our group reported 2,8-conjugation-extended anthradithiophene (**ADT**) polymers with cyclopentadithiophene (**CPDT**) as comonomers. These polymers form amorphous thin films and exhibit moderate charge transport with field-effect hole mobilities on the order of $10^{-3}$ cm$^2$ V$^{-1}$ s$^{-1}$. We also observed that the traditional, centrally bis-trialkylsilylethynylated **ADT**s, when incorporated in polymers, do not give rise to thin films with a high degree of molecular order. This contrasts with the crystallinity of the corresponding small molecule films. There could be two reasons for this observation. First, the bulky trialkylsilylethynyl groups on the central positions may sterically prevent backbones from approaching each other. Second, in the case of the **ADT**-containing systems, disorder is also likely introduced by the random orientation of the terminal thiophene rings due to a statistical sequence of syn- or anti-isomers arranged along the backbone (Chart 1a). The neighboring thiophene-terminated comonomers, e.g. **CPDT**, subsequently adopt random orientations to minimize local steric hindrance. This could potentially have formed a randomly-kinked backbone that makes it difficult to form ordered structures, in addition to randomly orienting sidechains which would have a very small chance of assisting main chain aggregation.
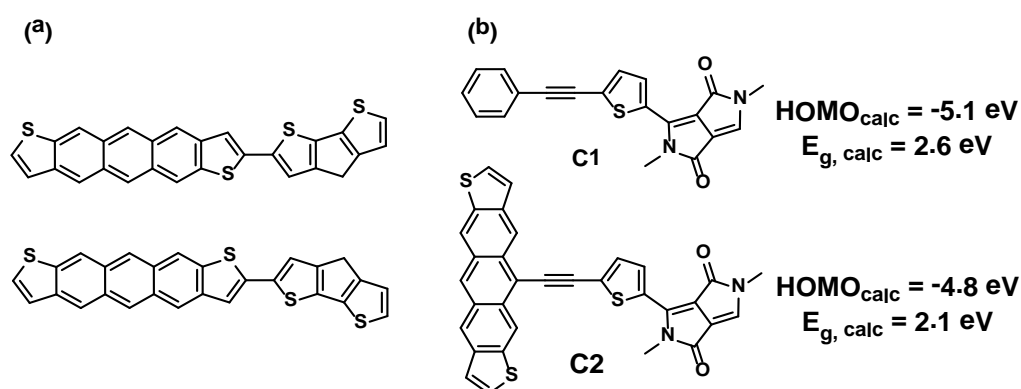


**(a)**

**(b)**

HOMO$_{calc}$ = -5.1 eV
E$_{g, calc}$ = 2.6 eV

**C1**

HOMO$_{calc}$ = -4.8 eV
E$_{g, calc}$ = 2.1 eV

**C2**

*Chart 1.* (a) Isomeric irregularities direct curvature along backbone; sidechains are omitted. (b) Analogous model compound units **C1** and **C2** for calculation (B3LYP/6-31G*); calculated HOMO energy levels and HOMO-LUMO gaps (E$_g$) are listed.

To address these two concerns, the molecular design approach taken in this work extends conjugation from the 5,11-positions of **ADT**, positioning **ADT** in the polymer backbone in an "orthogonal" fashion. This configuration greatly reduces the influence of the orientation of the terminal thiophene, and allows one to functionalize the 2,8-positions of **ADT** with linear sidechains, a versatile synthetic procedure to potentially induce closer packing of the polymer backbone, thus enhancing charge transport properties. The effect of π-stacks orthogonal to a polymer backbone has been reported in early efforts to synthesize low-bandgap polymers. In practice, while synthesis and characterization are known for polymers containing anthracene moieties with the long axis "orthogonal" to the polymer backbone, conjugated systems containing higher linear acenes are rare. Notable examples include a pentacene-fluorene random copolymer and 6,13-ethynylene-bridged pentacene oligomers, reported by Tokito and Lehnherr respectively. The former has a poor conjugation owing to steric repulsion between fluorene and pentacene units. The latter utilized acetylenic coupling over multiple synthetic steps to generate up to pentacene tetramers. In this work, we developed a facile route using *in situ* desilylation of the well-studied 5,11-bistrimethylsilylethynyl-**ADT** moiety, followed by palladium-catalyzed condensation of the arylalkynes with a dibrominated acceptor. Dithienodiketopyrrolopyrrole (**dTDPP**) was chosen, as it usually affords good charge transport properties in donor-acceptor systems. Calculations carried out for model compounds **C1** and **C2** (Chart 1b; details of frontal orbital visualization in Table S1 in supporting information), using Density Functional Theory, predicts that a 5,11-conjugation extended **ADT** (in compound **C2**) participates in conjugation with the backbone. As compared to **C1**, **C2** is expected to have a broader absorption spectrum (predicted optical E$_g$ listed in Chart 1b).

The proposed polymers based on the model units were synthesized according to Scheme 1. The reference polymer **Ph-dTDPP** was synthesized through Sonogashira coupling of the diethynylbenzene monomer **M1** and **dTDPP**, achieving a molecular weight ($M_n$) of over 18 kg mol-1. The target polymer, **oADT-dTDPP**, was synthesized from (1) *in situ* via desilylation of **M2** with tetrabutylammonium difluoro-triphenylsilicate (TBAT)

– a stable, solid-state source of fluoride ions that activate the silane; (2) a Sonogashira-type condensation with **dTDPP**. This synthetic route reproducibly yields **oADT-dTDPP** polymers with $M_n$ higher than 20 kg mol$^{-1}$, with a relatively high polydispersity index of 4.8 as measured by gel permeation chromatography (Table 1).
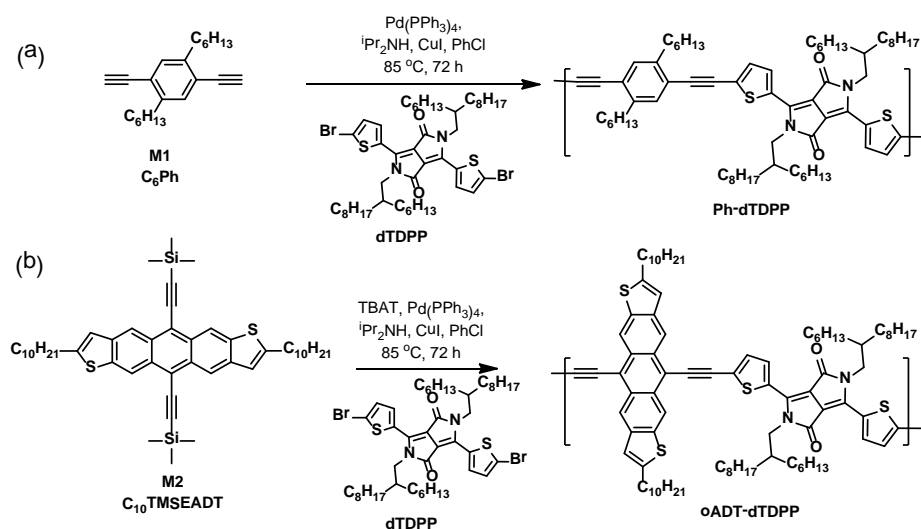


**Scheme 1.** Synthesis of (a) control polymer **Ph-dTDPP** via Sonogashira Coupling and (b) target polymer **oADT-dTDPP** via *in situ* desilylation.

The optical properties of **Ph-dTDPP** and **oADT-dTDPP** are summarized in Table 1 and Figure 1. In comparison with the monomers and **Ph-dTDPP**, **oADT-dTDPP**'s absorption in solution (Figure 1 inset), at around 910 nm, is largely red-shifted, absorbing primarily between 550 nm and 900 nm. From their molecular weights, it can be calculated that the batches of **Ph-dTDPP** and **oADT-dTDPP** possess approximately the same number of repeat units (15 to 18). Therefore, the red-shift of **oADT-dTDPP** by over 200 nm is likely a result of the orthogonal-**ADT**'s participation in conjugation with the backbone. To the authors' knowledge, this is the first example of an acene-containing low-bandgap alternating copolymer, with conjugation extended from the central rings. **oADT-dTDPP**'s small optical bandgap is reflected in its elevated HOMO level, as indicated by an early ionization onset at 5.0 eV, as measured by photoelectron spectroscopy of polymer films in air. This value is 0.4 eV smaller than that of **Ph-dTDPP**(Table 1). Finally, the absorption onset of **oADT-dTDPP** films is further red-shifted to around 950 nm (Figure 1) as compared to that of the polymer in solution, corresponding to an optical bandgap of 1.3 eV. The additional feature centered at 870 nm indicates further aggregation of the polymer chains in the solid state.

**Table 1.** Optical and electrochemical properties of **Ph-dTDPP** and **oADT-dTDPP**.

| Polymer | $M_n{}^a$ / PDI$^a$ (g/mol) | In solution | | | In film | |
|---|---|---|---|---|---|---|
| | | HOMO$^b$ (eV) | LUMO$^b$ (V) | $E_{g, opt}{}^c$ (eV) | $E_{onset}{}^d$ (eV) | $E_{g, opt}{}^c$ (eV) |
| **Ph-dTDPP** | 18700 / 3.5 | -5.20 | -3.41 | 1.80 | 5.41 | 1.60 |
| **oADT-dTDPP** | 23,500 / 4.8 | - | - | 1.36 | 5.00 | 1.30 |

$^a$Determined from GPC using THF soluble part. $^b$Determined from CV oxidation and reduction onsets in *o*-DCB with ferrocene as the standard. $^c$Estimated from the onset of film absorption. $^d$Determined from the onset of ionization of film in air.
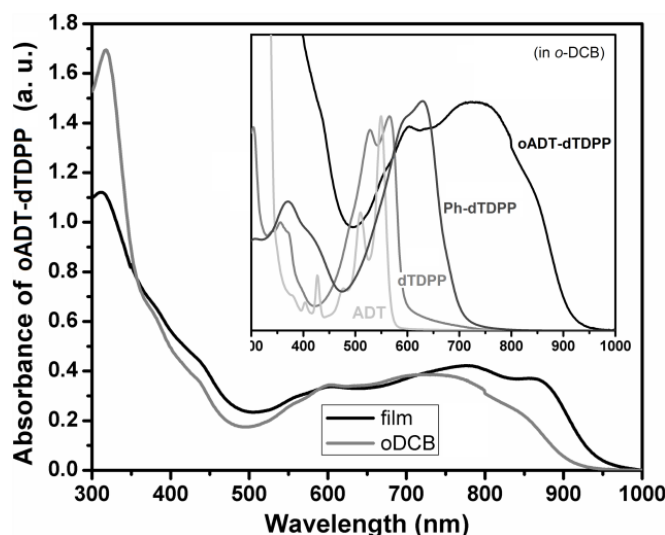
*Figure 1.* UV-Vis absorption spectra of **oADT-dTDPP** in thin-film and in *o*-DCB. The inset contrasts the absorption of the monomers and the polymers in *o*-DCB.

Grazing incidence X-ray diffraction (GIXD) studies performed on **oADT-dTDPP** thin films shows distinct out-of-plane (h00) Bragg peaks corresponding to polymer lamellae parallel to the substrate (Figure 2a), with a layer spacing of around 25 Å (Figure 2b). Such a clear indication of layer-like arrangement has not been observed with 2,8-conjugation-extended **ADT** polymers, where the bulky trialkylsilylethynyl groups are usually incongruent in volume and shape with the linear or branched side-chains on comonomers. In this case, the less bulky, linear chains on ADT may have helped to promote interchain interactions and the formation of lamellar order. In-plane diffraction intensity profile along qxy shows multiple poorly defined peaks with d-spacing from 3.6 – 5.5 Å. While the use of these to determine a unit cell is beyond the scope of this report, their presence indicates the existence of ordered domains within the film. This suggests that **ADT** units in the polymer orient with the long molecular axes perpendicular to the substrate, a motif that may give rise to better in-plane charge transport properties than previous less-ordered **ADT**-containing polymer systems.
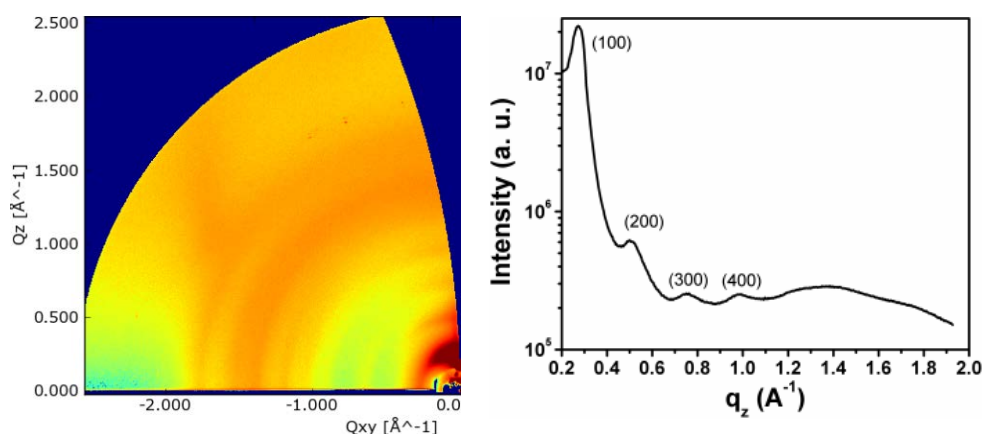


*Figure 2.* (a) GIXD diffraction pattern of (a) GIXD diffractogram of **oADT-dTDPP** thin film cast from PhCl annealed at 150 °C. (b) Out-of-plane diffraction intensity profile indicates a vertical lamellar spacing of around 25 Å.

Finally, the charge transport properties of **oADT-dTDPP** were investigated in the thin-film transistor (TFT) geometry. Solutions of **oADT-dTDPP** in chloroform ($CHCl_3$) and chlorobenzene (PhCl) were spin-cast onto octadecyltrichlorosilane-treated $SiO_2$ surfaces. The films were annealed at temperatures up to 210 °C, for 15 min, before gold source and drain electrodes were deposited. The TFT characteristics of the resulting devices

are listed in Table 2. PhCl proved to be a better processing solvent and yielded performance 30% to 50% higher than those of devices processed from $CHCl_3$. Hole mobilities up to 0.12 $cm^2$ $V^{-1}$ $s^{-1}$ were achieved. This value is two order of magnitude higher than those achieved by previous **ADT-CPDT** polymers and can likely be attributed to the improvement in thin-film packing and long-range order. Annealing the films at higher temperatures than 150 °C was found to degrade the hole transport properties of the material. Instead, an onset of weak electron transport was observed with mobilities on the order of $10^{-5}$ $cm^2$ $V^{-1}$ $s^{-1}$. The p-type transfer and output characteristics of PhCl-processed devices annealed at 150 °C are illustrated in Figure 3.

*Table 2.* Summary of **oADT-DTDPP**'s TFT charge transport properties for various device fabrication conditions. Average mobility values are tabulated, with maximum values in parentheses.

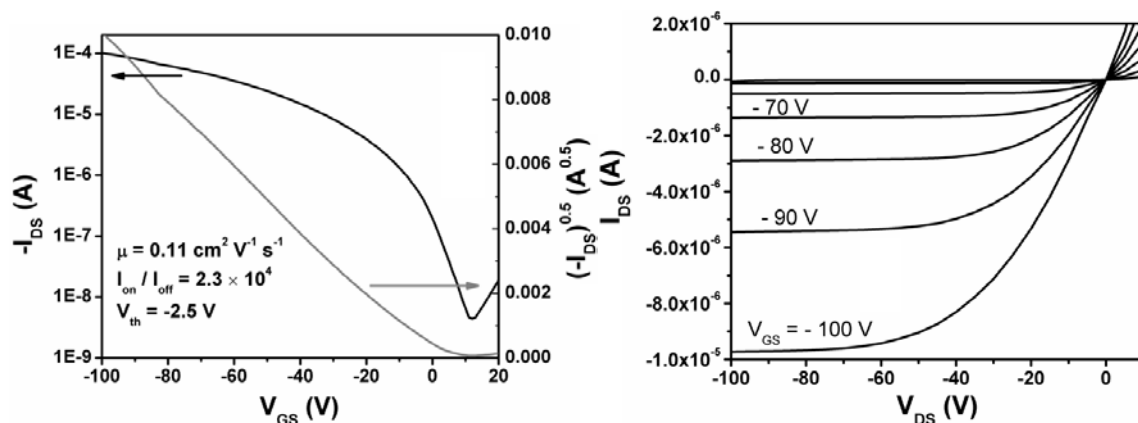| Solvent | $T_{anneal}$ (°C) | Hole or electron mobility, $\mu_h$ or $\mu_e$ ($cm^2$ $V^{-1}$ $s^{-1}$) | $I_{on}$ / $I_{off}$ | $V_{th}$ (V) |
|---|---|---|---|---|
| $CHCl_3$ | 150 | $\mu_h = 0.044 \pm 0.004$ (0.051) | $10^5$ | +2 ~ +20 |
| PhCl | | $\mu_h = 0.060 \pm 0.027$ (0.12) | $10^4 - 10^5$ | -10 ~ +10 |
| | 210 | $\mu_h = 0.007 \pm 0.001$ (0.009) | $10^4$ | -20 ~ +4 |
| | | $\mu_e = 2.7 \times 10^{-5} \pm 1.9 \times 10^{-5}$ ($4.8 \times 10^{-5}$) | $10^5$ | +30 ~ +60 |



*Figure 3.* P-type transfer and output characteristics of a representative **oADT-dTDPP** device spin-cast from PhCl on OTS-treated $SiO_2$, annealed at 150 °C.

In conclusion, the first 5,11-conjugation extended **ADT**-containing low bandgap polymer, **oADT-dTDPP,** is synthesized through a facile acetylenic coupling route. The expectation that an acene π-stack orthogonal to the polymer backbone delocalizes frontier electron densities was verified through molecular calculations and the synthesis of analogous polymers. Furthermore, **oADT-dTDPP** films were shown to contain lamellae oriented perpendicular to the substrate. Its TFT hole mobility reached 0.12 $cm^2$ $V^{-1}$ $s^{-1}$. This is the first time that an anthradithiophene-containing polymer film shows distinct ordered domains in the thin film, which resulted in much improved field effect transistor performance. This discovery suggests important guidelines on molecular designs to future higher performing functional acene-containing polymers.

## 4. Controlling Electric Dipoles in Nanodielectrics and Its Applications for Enabling Air-Stable n-channel Organic Transistors

Manipulating the channel charge density of transistors is important to maximize their functionality. In conventional silicon, germanium, and III-V semiconductor devices, the amount of charge carriers can be

precisely controlled through doping; however, the development of a suitable doping method for accurate control of charge carriers has proven to be relatively difficult for novel semiconductors such as π-conjugated organic semiconductors, carbon nanotubes, and graphene. Here, we introduce a method to control electric dipoles using self-assembled monolayers (SAMs) with different anchor groups. We utilized the SAM dipoles in the nanodielectric of organic field-effect transistors (OFETs) and successfully adjusted the energy levels of electrons in the channel, which in turn resulted in a significant change in the transistor turn-on voltage. Moreover, this tuning of electron energy levels can significantly improve the performance of n-channel (electron-conducting) OFETs, which are generally not stable in air. These changes in the electrical properties of the transistors were made without alteration to the desirable head group of the SAMs that is crucial for optimal growth of the organic semiconductors. We believe that the findings here can also be applied to controlling the electrical properties of other nanoelectronic devices.

Previously, several research groups demonstrated the use of SAMs to control the threshold voltage of OFETs. SAMs have also been used to control the Schottky barrier between organic semiconductors and metals. However, in these previous studies, the common approach to control the electrical properties has been to use electron-withdrawing or -donating head groups of the SAMs. As previous reports showed that the mobility of organic transistors can vary by an order of magnitude with different head groups, the chemical moieties at the surface of a SAM can significantly impact the morphology and the charge transport of the subsequently deposited semiconductor. Moreover, some head groups may transfer charges to the semiconducting layer, and these charges can change the threshold voltage. Thus, the SAM dipoles are insufficient to explain the voltage shifts in these previous studies although several groups have attempted to interpret the shifts using the SAM dipoles. To date, no experimental demonstration has been reported to explain accurately the voltage shifts caused by the SAMs.

In this study, we utilized octadecylphosphonic acid (OPA) and octadecylsilane (OTS) to form the SAM, as shown in Fig. 1a. These two molecules have the same methyl head group and alkyl chain. Therefore, the OPA and OTS SAMs are appropriate to study the influence of SAM-induced electric dipoles without the secondary effects mentioned above. Previous works have demonstrated the usage of both SAMs in the gate dielectric of OFETs. However, we found that the OPA and OTS SAMs on aluminum oxide ($AlO_X$) generated different dipole-moment directions and built-in voltages, entirely due to the difference of the anchor groups. For the OPA SAM, the measured dipole moment pointed away from the SAM-$AlO_X$ interface, whereas the direction of the dipole moment for the OTS SAM was measured to be opposite.

The poor stability of n-channel OFETs is mainly due to the presence of electron traps in air. As most thin-film organic semiconductors are sensitive to chemicals and high temperature, and are mechanically weak, the bottom-gate geometry is generally used in OFETs. Therefore, electrons in n-channel OFETs can be quenched by electron traps in air if the electron affinity, i.e. the difference between the vacuum level and the lowest unoccupied molecular orbital (LUMO), of the semiconductor is less than that of the respective trap states. In spite of a great deal of effort devoted to increasing the electron affinity of organic semiconductors, so that they are not affected by such traps, only few materials showed mobilities greater than 1 $cm^2$/V·s in n-channel OFETs measured in air.

The OFET structure used in this study is shown in Fig. 1b. The capacitance values of the OPA/$AlO_X$ and OTS/$AlO_X$ dielectrics were 0.455 (±0.004) μF/$cm^2$ and 0.465 (±0.001) μF/$cm^2$, respectively. The static contact angle of water for both SAMs was 106° while that of the $AlO_X$ was only 9°. The root-mean-square roughness of the $AlO_X$ and both SAMs was measured to be 0.2 nm, which was identical to that of the silicon substrate, by atomic force microscopy (AFM). Grazing incidence X-ray diffraction (GIXD) revealed that the OPA and OTS SAMs were crystalline with nearly identical packing structure, as evidenced by the presence of a Bragg rod at $Q_{xy}$ = 1.49 Å$^{-1}$ for both SAMs. This feature is indicative of a crystalline monolayer with a 4.2 Å hexagonal lattice constant. From X-ray reflectivity (XRR) measurements, the packing densities of the OPA and OTS SAMs were calculated as 4.55 (±0.16) and 5.36 (±0.64) molecules per n, respectively. These density values are quite similar to the results from earlier studies: 4.6 molecules per $nm^2$ (OPA SAM on $AlO_X$) and 5.0 molecules per $nm^2$ (OTS SAM on silicon dioxide). Previously, we found that crystalline OTS SAM promoted a 2-dimensional growth of organic semiconductors and generally resulted in higher-mobility OFETs, compared to those fabricated on less dense and amorphous OTS SAMs.
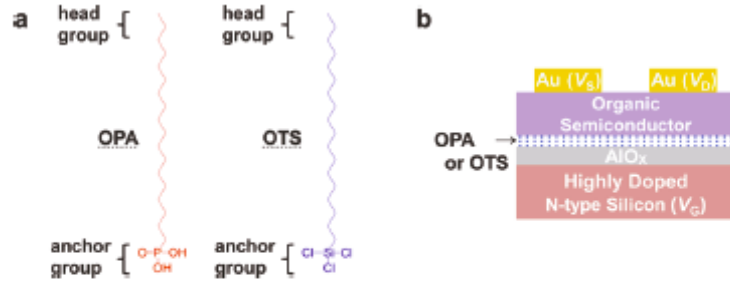
Figure 1. (a) Chemical structures of SAM molecules and (b) a schematic of OFETs.

We fabricated buckminsterfullerene (C60), $N,N'$-ditridecyl-3,4,9,10-perylenetetracarboxylic diimide (PTCDI-C13), and pentacene OFETs on OPA/AlO$_X$ and OTS/AlO$_X$ gate dielectrics. Their current-voltage characteristics were first measured in a nitrogen atmosphere. Figure 2a shows the drain current ($I_D$) vs. gate-source voltage ($V_{GS}$) curves in saturation mode. For all three types of OFETs similar amounts of negative voltage shifts were observed in the $I_D$-$V_{GS}$ curves for the OPA/AlO$_X$ gate dielectric compared to the OTS/AlO$_X$ case. In order to quantify the voltage shifts, we compared the turn-on voltage ($V_{ON}$), which we define as the $V_{GS}$ where the first derivative of $I_D$-$V_{GS}$ curve is zero. [The threshold voltage ($V_{TH}$), defined as a fitting parameter in equation (1), depends on the mobility ($\mu_{FET}$) and does not have a clear physical meaning in organic transistors[23]. Since the effects of dipoles on the energy levels in the channel region were studied here, the turn-on voltage ($V_{ON}$) was measured, as it indicates when the channel is the most depleted in OFETs.]

$$I_{D,SAT} = \frac{W}{2L} \times \mu_{FET} \times C_g \times \left(V_{GS} - V_{TH}\right)^2 \quad (1)$$

($W$: channel width, $L$: channel length and $C_g$: gate capacitance)

The $V_{ON}$ values for OPA/AlO$_X$ were always measured to be more negative than those for OTS/AlO$_X$, as summarized in Fig. 2b: C60 (-0.35 V), PTCDI-C13 (-0.35 V), and pentacene (-0.38 V).

In order to extract flatband voltage ($V_{FB}$) values, we conducted capacitance-voltage ($C$-$V$) measurements on pentacene metal-insulator-semiconductor (MIS) devices in a nitrogen atmosphere. As shown in Fig. 3, the average difference in $V_{FB}$ between OPA/AlO$_X$ and OTS/AlO$_X$ was 0.41 V, which is close to the $V_{ON}$ differences. These $V_{FB}$ results and the voltage shifts in the $I_D$-$V_{GS}$ curves imply that the energy levels of electrons in the channel region for OPA/AlO$_X$ are lower than those for OTS/AlO$_X$.

We monitored the stability of C60 and PTCDI-C13 OFETs on both types of gate dielectrics over an extended period in air (see Fig. 4). The n-channel OFETs on the OPA/AlO$_X$ gate dielectric showed much less degradation than those on the OTS/AlO$_X$ gate dielectric. For the transistors on the OTS/AlO$_X$ gate dielectric, the mobility was observed to drop by more than one order of magnitude after only two days in air. The decrease was accompanied by an increase in the corresponding threshold voltage, which resulted in a parallel shift in the $I_D$-$V_{GS}$ curves. However, for the OPA/AlO$_X$ gate dielectric, the mobility of C60 OFETs was observed to change only slightly from 1.69 ($\pm$0.14) to 1.65 ($\pm$0.11) cm$^2$/V·s after 24 hours and maintained at 0.73 ($\pm$0.06) cm$^2$/V·s even after one week in air. The mobility of PTCDI-C13 OFETs on the OPA/AlO$_X$ gate dielectric was measured to be still 0.09 ($\pm$0.03) cm$^2$/V·s after one week exposure in air.
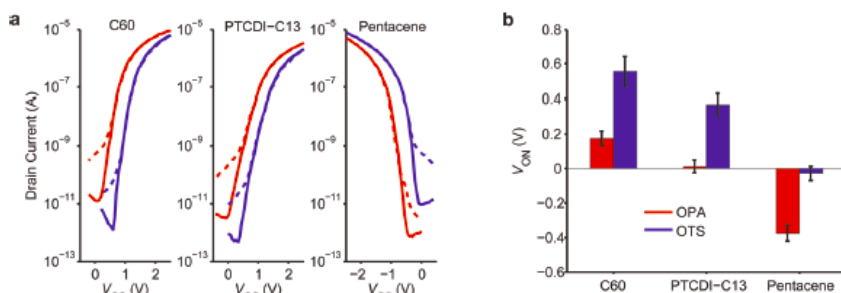
**Figure 2.** $I_D - V_{GS}$ and $V_{ON}$ data of OFETs (saturation mode, $V_{DS} = \pm 2.5$ V) measured in a nitrogen atmosphere. (a) The red lines represent the data from OPA/AlO$_X$, and the blue lines are the data from OTS/AlO$_X$ (solid lines, forward sweep; dotted lines, backward sweep). (b) Average $V_{ON}$ data of OFETs on OPA/AlO$_X$ and OTS/AlO$_X$. The error bars represent standard deviations.
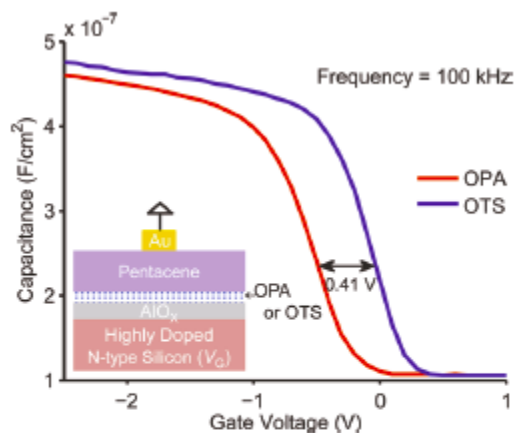


**Figure 3.** $C-V$ data of pentacene MIS structure measured in a nitrogen atmosphere. The schematic is the MIS structure used in the measurements. A 100 kHz ac signal of 10 mV was applied to the bottom-gate silicon electrode.

We examined the morphologies of organic thin films on OPA and OTS using GIXD and AFM to determine if morphological differences could contribute to improved air stability when using the OPA/AlO$_X$ gate dielectric. GIXD and AFM results indicate that the morphologies of C60 and PTCDI-C13 thin films are nearly identical on the OPA and OTS SAMs. The GIXD images of the C60 thin films displayed predominantly isotropic crystallite orientations, and GIXD of the PTCDI-C13 thin films showed well-ordered crystalline morphologies. Further details on the morphological characterization can be found in the supporting information.
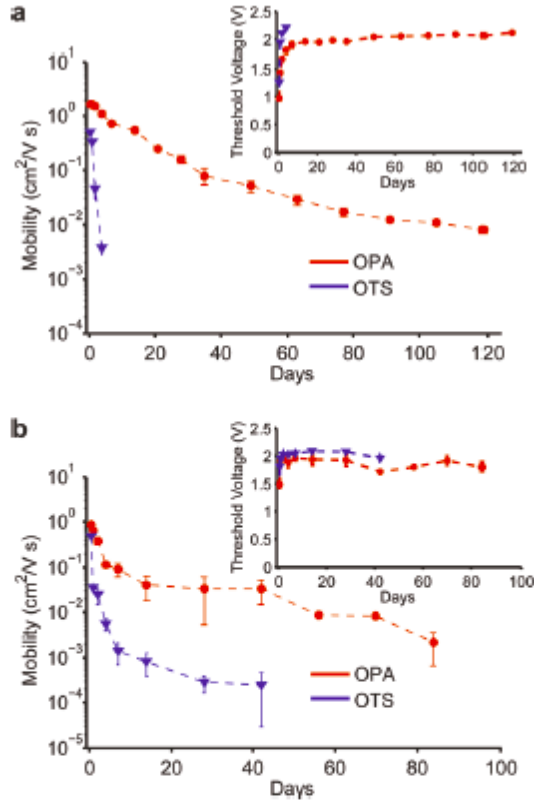
**Figure 4.** Long-term stability of (a) C60 and (b) PTCDI-C13 OFETs in air. The OFETs were tested in saturation mode, and the mobility and threshold voltage parameters were extracted from eq 1. The OFETs on OTS/AlO$_X$ did not show any modulation of drain current by the gate voltage after 1 week (C60) and 6 weeks (PTCDI-C13) exposure in air, while the OFETs on OPA/AlO$_X$ had $I_{ON}/I_{OFF}$ ratios of more than $10^3$ after 17 weeks (C60) and 12 weeks (PTCDI-C13) in air.

The effects of SAM dipoles in the MIS structure are described in Fig. 5, where the built-in potential generated by the dipoles ($V_{SAM}$) is modeled as a DC battery. With the polarity of dipole in this example, the SAM dipoles accumulate electrons at the dielectric-semiconductor interface by lowering the electron energy levels of the semiconductor. In order to remove the accumulated charges, an external voltage of the same magnitude as the $V_{SAM}$ with the opposite polarity needs to be applied at the gate. When this voltage (-$V_{SAM}$) is applied, the accumulated charges are removed, and this state is defined as the flatband condition. Using the same analogy, the voltage shifts in the $I_D$-$V_{GS}$ and $C$-$V$ curves due to the SAM dipoles can be estimated as -$V_{SAM}$. In order to check the validity of the explanation, we varied the thickness of the AlO$_X$ layer and measured the $V_{ON}$ difference of pentacene OFETs between the OPA/AlO$_X$ and OTS/AlO$_X$ gate dielectrics in a nitrogen atmosphere. As shown in Table 1, the difference of $V_{ON}$ between OPA/AlO$_X$ and OTS/AlO$_X$ did not depend on the thickness of the gate dielectric.
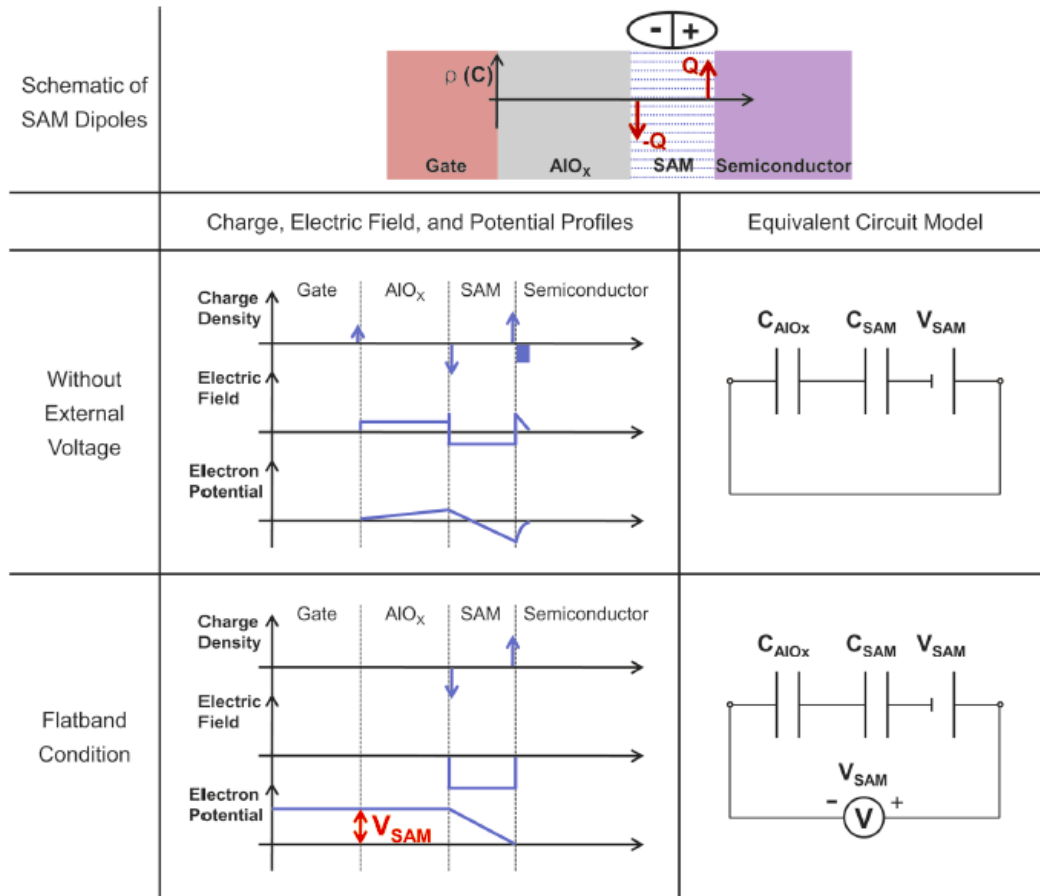
Figure 5. Effects of SAM dipoles in the MIS structure. In this analysis it is assumed that the flatband voltage without the dipoles is zero.

| Gate Dielectric | 4.5 nm AlO$_X$ | | 9.5 nm AlO$_X$ | |
| --- | --- | --- | --- | --- |
| | OPA SAM | OTS SAM | OPA SAM | OTS SAM |
| Capacitance (μF/cm$^2$) | 0.455 (±0.004) | 0.465 (±0.001) | 0.328 (±0.002) | 0.334 (±0.007) |
| $V_{ON}$ (V) | -0.38 (±0.05) | -0.03 (±0.04) | -0.55 (±0.06) | -0.18 (±0.03) |
| $\Delta V_{ON}$ (V) | 0.35 | | 0.37 | |

**Table 1.** $V_{ON}$ data of pentacene OFETs (saturation mode) with different AlO$_X$ thickness, measured in a nitrogen atmosphere.

   In previous publications, a different interpretation about the voltage shifts by SAM dipoles was offered. The authors asserted that an electric field created by a SAM should be eliminated by external voltage in order to compensate the voltage shift from the dipoles: $-E_{SAM} \times d$ ($E_{SAM}$: built-in electric field of SAM and $d$: gate dielectric thickness). However, as Fig. 5 shows, the accumulated charges due to the SAM dipoles are removed simply by applying the opposite voltage of the built-in potential of the SAM ($-V_{SAM}$), not by removing the electric field.

   The $V_{SAM}$ generated by OPA and OTS SAMs can be measured directly through modification of aluminum work function. Since the surface of aluminum rapidly oxidizes once exposed to air, the influence of the SAM dipoles on aluminum is nearly identical to the influence on AlO$_X$. We observed that the OPA SAM lowered the work function of aluminum by -0.27 eV, while the OTS SAM raised the aluminum work function by +0.23 eV. This result suggests that the surface potential of the OPA-treated AlO$_X$ is 0.50 V higher than the OTS-treated AlO$_X$, which is comparable to the voltage shifts in the $I_D$-$V_{GS}$ and $C$-$V$ curves. The only difference between the OPA and OTS molecules is their anchor groups, bound to the surface. Thus, our work function data indicate that the chemical bonding of the SAMs to the oxide surface can have a significant effect on the overall dipoles.

   N-channel OFETs on OPA/AlO$_X$ are less impacted by the electron traps in air than those on OTS/AlO$_X$, due to the lowered electron energy levels in the channel (see Fig. 6). This lowering of the energy levels by the OPA dipoles is equivalent to the increase in the electron affinities of organic semiconductors, which enables air-

stable n-channel operation. The performance of n-channel OFETs made of C60 and PTCDI-C13 has been known to rapidly degrade in air due to their low electron affinities. Previously, C60 and PTCDI-C13 OFETs with mobility values of greater than 1 cm$^2$/V·s have only been reported in an inert environment. However, by using the OPA/AlO$_X$ gate dielectric, the energy levels of electrons in the channel are lowered by the dipoles. Thus, the driving force for trapping electrons is weakened, and the air stability of n-channel organic transistors is significantly improved.

In conclusion, we manipulated the electric dipoles in the gate dielectric by using SAMs with different anchor groups. The different dipoles between the OPA and OTS SAMs resulted in significant voltage shifts in the $I_D$-$V_{GS}$ and $C$-$V$ curves of organic transistors. Through the effects of dipoles, we suppressed the trapping of electrons due to air exposure and greatly enhanced the air stability of existing organic semiconductors in n-channel OFET applications. The potential difference caused by the OPA and OTS SAMs on AlO$_X$ was measured to be 0.41–0.50 V. It is likely that this difference may dependent on the SAM preparation conditions and substrate used. Further investigation is needed to understand the origin of the difference in the dipole. In nanoelectronics, where low voltage is generally used, such potential difference can greatly modify the electrical characteristics of the devices. Therefore, the OPA and OTS SAMs on AlO$_X$ can be utilized in nanoelectronic devices composed of other semiconductor materials—for which a precise method of doping does not exist—to induce different electric potentials while maintaining nearly identical interface between the SAMs and the semiconducting layer.
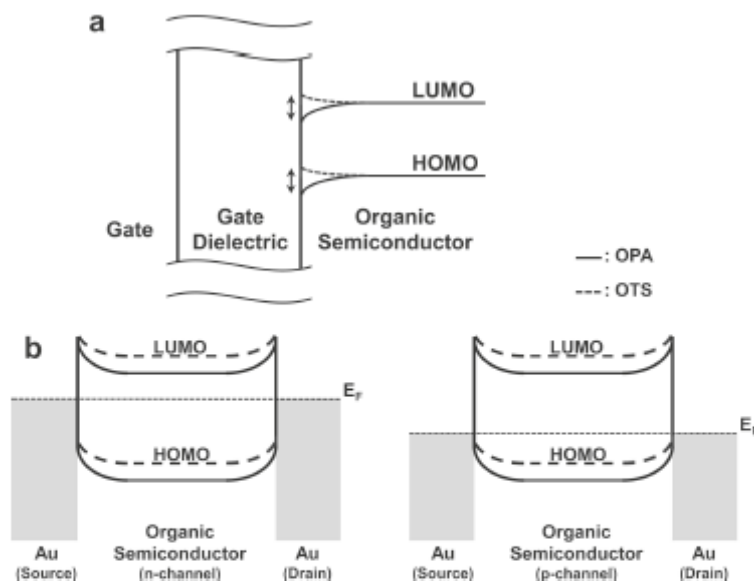


**Figure 6.** Qualitative description of energy band diagrams (a) in the gate-to-channel direction and (b) in the horizontal direction from the source to the drain electrodes. Due to the different dipole moments, the lowest unoccupied molecular orbital (LUMO) and the highest occupied molecular orbital (HOMO) levels are split at the dielectric—semiconductor interface between OPA/AlO$_X$ and OTS/AlO$_X$.

## 4. A method to achieve high mobility aligned crystals from solution

We designed a simple droplet-pinned crystallization (DPC) method (Fig. 1a) to prepare well aligned C$_{60}$ crystals. The operating principle of this approach is as follows: During drying of a droplet of a semiconductor solution on a substrate, crystals nucleate near the contact line and grow along the receding direction (towards the centre) of the droplet. Using this method, well-aligned C$_{60}$ needle and ribbon crystals were prepared (Fig. 2a, d).

During the DPC process, the shape, size, and location of the droplet are determined by those of the pinner, which gives the DPC method several remarkable advantages. Firstly, DPC is easily scalable. The pinners can be patterned over a large area with a controlled density. We scaled the processed area up to a 100 mm wafer area (Fig. 1b, Fig. 3). Around 50% of the wafer surface was covered by aligned crystals. This area fraction will further increase if we decrease the size of the pinners. We envision that an even larger processed area should be achievable. Secondly, DPC can be used to define the location of the aligned crystals, which is important towards making complex circuits. Since the locations of the droplets are dictated by our pinners, we could therefore achieve crystallization of desired patterns (Fig. 1b, Fig. 3). Based on our DPC method, we have been able to position both p- and n-channel organic semiconductors on a common substrate to fabricate complimentary circuits.
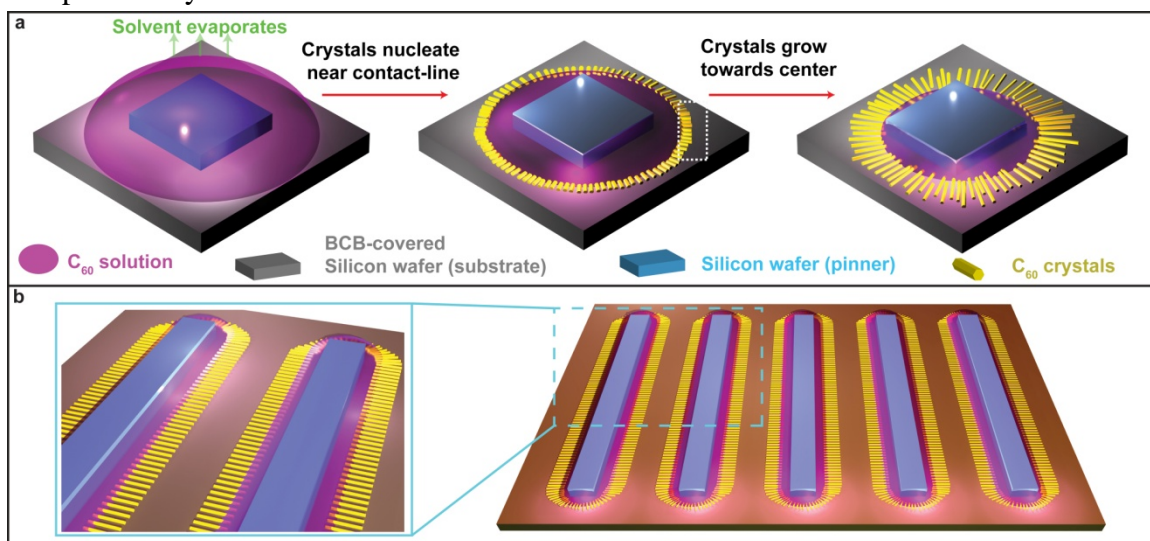


Figure 1: Schematic representations of the DPC method. (a) An organic semiconductor droplet pinned by a silicon wafer. As the solvent evaporates slowly, the crystals of the organic semiconductors nucleate near the contact line of the droplet. Subsequently, the nuclei grow along the receding direction (towards the centre) of the droplet. (b) DPC can be scaled up by using multiple pinners with larger sizes. Elongation of the pinner leads to unidirectional parallel alignment of the crystals.
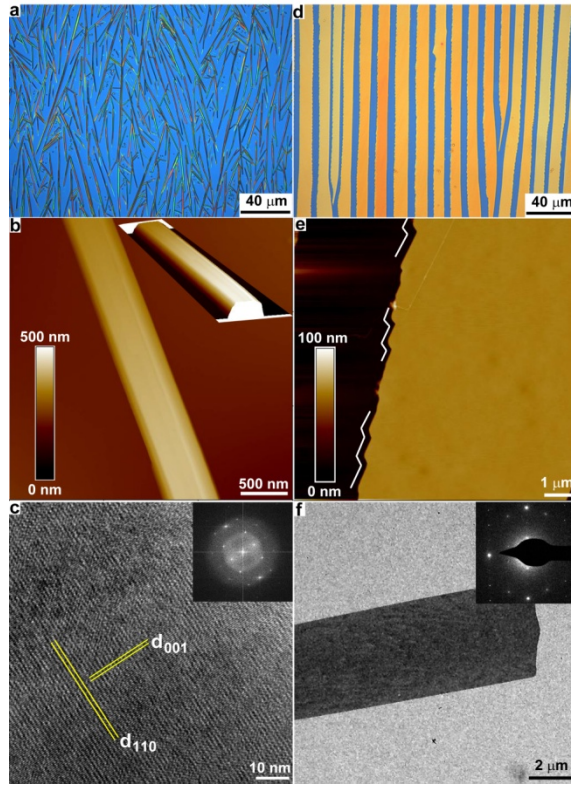
Figure 2: Morphologies and crystalline structures of well-aligned C60 needle (a-c) and ribbon (d-f) crystals prepared by the DPC method. (a, d) Optical microscopy (OM) images of well-aligned C60 needle and ribbon crystals. (b) A AFM image of a needle crystal showing faceted shape. (Inset) a 3-D view of image (b). Height of 20 needle crystals was measured, giving an average of $175 \pm 80$ nm (SD). (c) A high-resolution TEM image of a needle crystal, showing a regular 2-D lattice viewed down the $[1\bar{1}0]$ zone axis of C60•m-xylene single-crystals. (Inset) Fast Fourier transform (FFT) of (c). (e) A AFM image of a ribbon crystal. White lines highlight the faceted edges. Height of 10 ribbon crystals was measured, giving an average of $57 \pm 7$ nm (SD). (f) A TEM image of a ribbon. (Inset) A SAED pattern containing a single set of spots, indicating the single-crystallinity of the ribbon. SAED at different locations of the ribbon showed identical patterns.
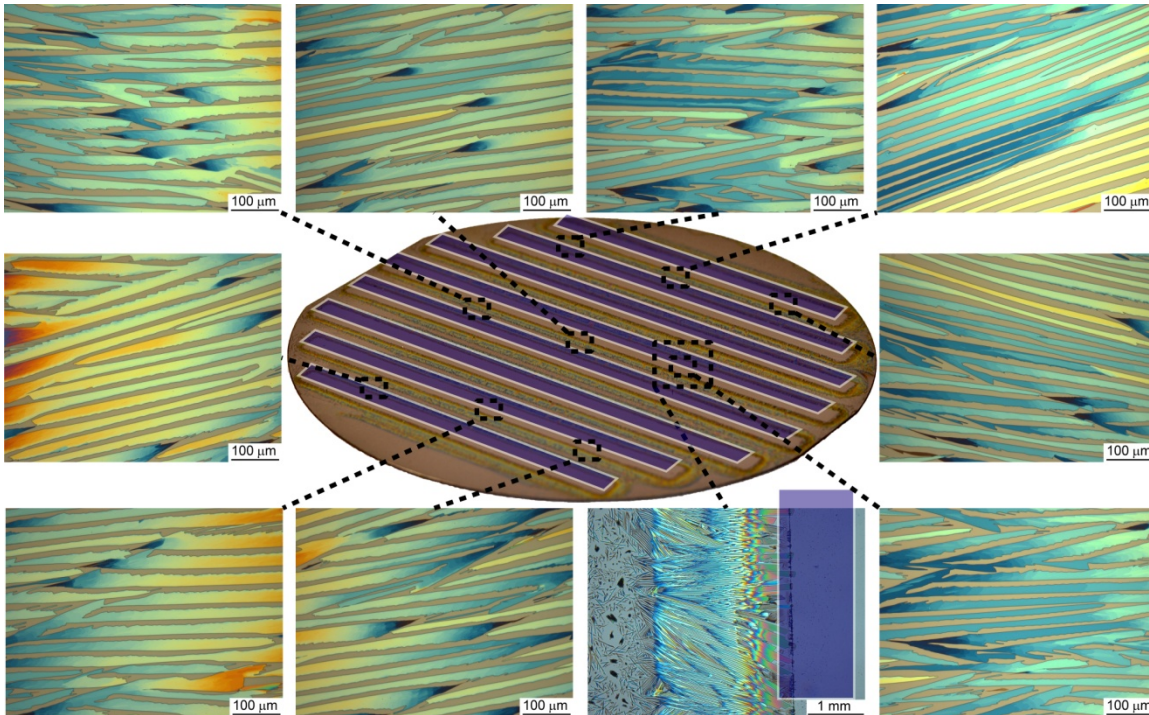


**Figure 3:** OM images of horizontally-aligned ribbon crystals grown on a 100 mm silicon wafer. A image of the wafer is shown in the middle. The stripe-pattern, highlighted in purple, is where we placed the silicon pinners to direct the crystal alignment. Across the wafer, crystals are aligned roughly perpendicular to the long-axis of the pinners.

After obtaining the crystals, we proceed to characterize the morphologies and crystalline structures of the crystals. $C_{60}$ needle crystals were grown from a solution of m-xylene on divinyltetramethyldisiloxane bis(benzocyclobutene) (BCB)-covered $SiO_2$/Si substrates (Fig. 2a). Previously, crystals grown from the same solvent on $SiO_2$/Si substrates exhibited a similar needle shape, albeit without alignment. Here, by using DPC, we obtained well-aligned crystals with lengths up to 200 μm (Fig. 2a). Instead of a bare $SiO_2$/Si substrate, we used thermally cross-linked BCB to eliminate the electron traps arising from the surface hydroxyl group on $SiO_2$. Atomic force microscopy (AFM) shows a faceted shape and very smooth surfaces (rms roughness ~1 nm) from the needles (Fig. 2b), indicative of crystalline structures. This was further confirmed by transmission electron microscopy (TEM). TEM shows a regular two-dimensional (2-D) lattice image viewed down the [1$\bar{1}$0] zone axis of $C_{60}$ single-crystals (Fig. 2c). The crystalline structure is consistent with the previously-reported hexagonal structure of $C_{60}$•m-xylene crystals grown from the same solvent.

Besides the needle-shaped crystals, well-aligned ribbon crystals were also prepared from a mixture of solvents (m-xylene and carbon tetrachloride ($CCl_4$)). The flat 2-D ribbon-shaped crystals promise a higher current output from the resulting FETs as they have a larger contact area (with the electrodes and the dielectric of the devices), compared to the needle crystals discussed earlier. We used mixed solvents to optimize the shape and coverage of the crystals. With a volume ratio of 4:3 ($CCl_4$ : m-xylene), long ribbons of several hundred microns in length were obtained with thickness of $57 \pm 7$ nm (Fig. 2d,e and Fig. 3). AFM images show faceted edges (Fig. 2e, white lines) and smooth surfaces with a rms roughness (~0.15 nm) much smaller than the diameter of $C_{60}$ molecules (~0.7 nm). These faceted morphologies imply single-crystallinity that is further confirmed by selected area electron diffraction (SAED) showing a single set of spots (Fig. 2f). SAED patterns from multiple areas of the same ribbon are identical, supporting the single-crystalline nature.

We characterized field-effect transistors (FETs) based the $C_{60}$ crystals. The alignment facilitates FET fabrication as electrodes can be easily deposited perpendicular to the aligned crystals. FETs were constructed based on the well-aligned needles and ribbons in a bottom-gated configuration, by depositing Au top-contact source and drain electrodes, with channel length (L) of 50 μm and width (W) of 1 mm (Fig. 4a, b inset, and d). For each type of crystals, 60 devices from 4 substrates were tested under $N_2$ atmosphere and the saturation regime electron mobility was calculated. The typical transfer characteristics of the devices are shown in Figure 4b and e, exhibiting excellent gate modulation. Since the crystals do not fully cover the channels, the active channel width was measured from the contacting area of the crystals that cross the source and drain electrodes (Fig. 4a and d). For the needles, an average electron mobility ($\mu$) of $5.2 \pm 2.1$ cm$^2$V$^{-1}$s$^{-1}$ (Fig. 4c), on-to-off current ratios ($I_{on}/I_{off}$) > $10^5$ and threshold voltages ($V_T$) between 15 to 43 V were achieved. For the ribbons, average $\mu$ of $3.0 \pm 0.87$ cm$^2$V$^{-1}$s$^{-1}$ (Fig. 4f), $I_{on}/I_{off}$ > $10^6$ and $V_T$ between 36 to 85 V were obtained. The variations of the $\mu$ and $V_T$ values are associated with the slightly different orientation of the crystals with respect to the electrodes, and can be minimized by reducing channel geometry (W and L). We also assessed the bias stress effects of the devices. Transfer characteristics were recorded before and after the devices were biased in the "on" state for one hour. The extracted $\mu$ and $V_T$ values before and after bias stress show a small variation below 10%.
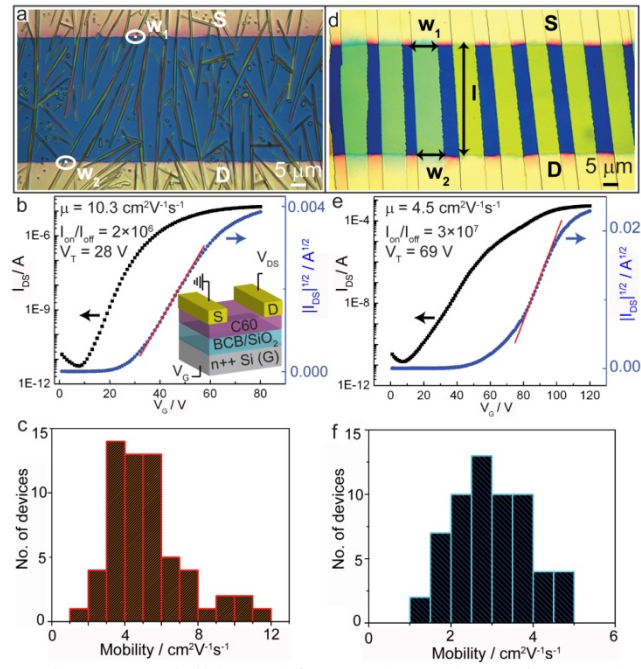
**Figure 4:** FET characteristics of $C_{60}$ needle (a-c) and ribbon (d-f) crystals. (a, d) OM images showing crystals between source (S) and drain (D) electrodes. The active charge transport channel dimensions (W and L) were corrected by the equations: $W = \Sigma(w_1+w_2)/2$; $L = l$. L was measured from the real channel length and W was measured from the contacting area of the crystals that cross the S and D electrodes. (b, e) Typical transfer characteristics. Inset: a schematic representation of the FET configuration, where S is the source, D the drain and G the gate. Device characteristics ($\mu$, $I_{on}/I_{off}$ and $V_T$) are also shown. The $\mu$ is calculated using the corrected W and L. For the device shown in (b), W/L = 8.7 μm/40 μm; for (e), W/L = 817 μm / 47 μm. (c, f) Histogram of the electron mobility calculated using corrected W and L from 60 devices.

We used the droplet-pinned crystallization (DPC) method again to grow TIPS-pentacene crystals. TIPS-pentacene ribbons were grown from a solution of a mixed solvent (m-xylene and carbon tetrachloride ($CCl_4$), volume ratio 1:1) on a divinyltetramethyldisiloxane-bis(benzocyclobutene) (BCB)-covered $SiO_2$/Si substrate (Fig. 5A). Individual ribbons show the same color and brightness between crossed-polarizers and extinguish simultaneously as single crystals when they are rotated (Fig. 5B). Grazing X-ray diffraction (GIXD) pattern indicated that the ribbons were (001) oriented TIPS-pentacene crystals (Fig. 5C). Atomic force microscopy (AFM) showed a faceted shape and a step-terrace geometry, indicative of single-crystallinity (Fig. 5D-F). The step height is 1.64 nm, close to 1.65 nm of the (001) d-spacing, which reconfirms that the (001) planes are parallel to the substrate plane. The thickness of the ribbons is $42 \pm 9$ nm measured by AFM. Nano-particles were found on the crystal surfaces, especially at the step edges (Fig. 5E, F). They are likely from impurities expelled by the growing crystals. TIPS-pentacene single-crystals with the similar ribbon morphology and crystalline orientation were previously grown from solutions, albeit without alignment. Also aligned TIPS-pentacene crystals showing hole mobility below 1 $cm^2V^{-1}s^{-1}$ were reported, with twinning defects. Here, the alignment induced by DPC will facilitate FET fabrication and the single-crystallinity promises higher mobility.
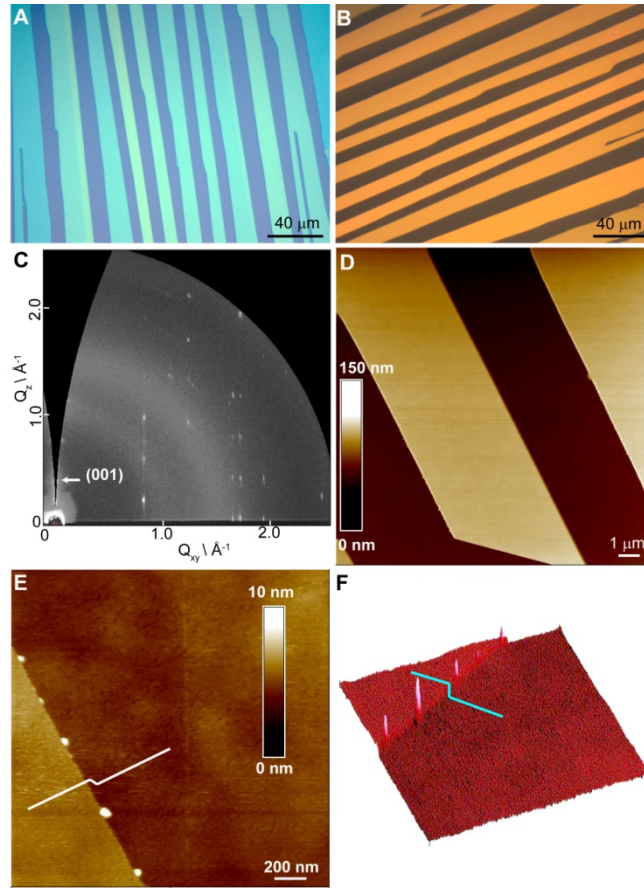
Figure 5: Morphologies and crystalline structures of well-aligned TIPS-pentacene crystals prepared by the DPC method. (A) An OM image of the crystals, showing the alignment of the ribbons. (B) An OM image of the crystals between crossed-polarizers, showing the uniform color and brightness throughout the crystals. (C) A GIXD pattern of the crystals. The out-of-plane (00l) peaks indicate the crystals are (001) oriented. (D) A AFM image of the crystals, showing the faceted shape and smooth surface. (E) A AFM image of a higher magnification, showing the step-terrace geometry. Nano-particles at the step edge are also seen. (F) A 3-D view of image (E).

FETs were constructed in a top-contact, bottom-gate configuration, by depositing Au source and drain electrodes, with channel length (L) of 50 μm and width (W) of 1 mm. 50 devices from 3 substrates were tested under $N_2$ atmosphere and the saturation regime electron mobility was extracted. Figure 6A and B show the typical transfer and output characteristics of the devices, exhibiting excellent gate modulation. An average hole mobility (μ) of $1.5 \pm 0.5$ cm$^2$V$^{-1}$s$^{-1}$ (range 0.8-2.8 cm$^2$V$^{-1}$s$^{-1}$, Fig. 6C), on-to-off current ratios ($I_{on}/I_{off}$) > 105 and threshold voltages ($V_T$) between -6 to -35 V were achieved. Since the crystals do not fully cover the channels, the active channel width was corrected to calculate the mobility of the crystals by measuring the contacting area of the crystals that cross the source and drain electrodes (Fig. 6D, inset). An average corrected hole mobility ($\mu_{correctted}$) of $2.4 \pm 0.6$ cm$^2$V$^{-1}$s$^{-1}$ (range 1.6-3.8 cm$^2$V$^{-1}$s$^{-1}$, Fig. 6D). The highest hole mobility we achieved is 3.8 cm$^2$V$^{-1}$s$^{-1}$ , which is remarkably higher than the previously-reported mobility of TIPS-pentacene thin films and single-crystals (below 1.8 cm$^2$V$^{-1}$s$^{-1}$). We attribute the high mobility to the single-crystallinity and the crystal alignment.
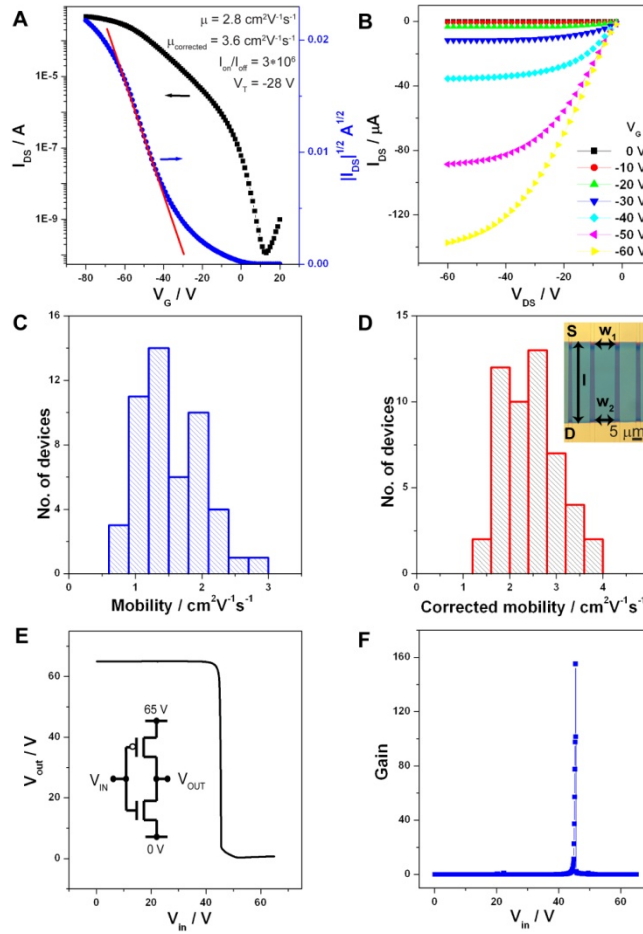
Figure 6: FET and inverter characteristics. (A, B) Typical transfer and output characteristics of the FETs based on TIPS-pentacene single-crystals. Device characteristics ($\mu$, $I_{on}/I_{off}$ and $V_T$) are shown in (A). (C) Histogram of the hole mobility of 50 TIPS-pentacene FETs. (D) Histogram of the hole mobility calculated using corrected W/L from the 50 devices. Inset: an OM image showing the method of W/L correction. The active charge transport channel dimensions (W and L) were corrected by the equations: W = ($w_1$+$w_2$)/2; L = l. L was measured from the real channel length and W was measured from the contacting area of the crystals that cross the source (S) and drain (D) electrodes. (E, F) The switching characteristic (E) and the corresponding gain (in absolute value) (F) of a inverter comprised of p-channel TIPS-pentacene and n-channel $C_{60}$ crystals. Inset: the inverter circuit configuration.

After obtaining p-channel TIPS-pentacene FETs, we proceeded to prepare complimentary inverters. We selected our previously-reported $C_{60}$ ribbon single-crystals for the n-channel FETs (average electron mobility $2.0 \pm 0.61$ cm$^2$V$^{-1}$s$^{-1}$). $C_{60}$ and TIPS-pentacene aligned single-crystals were grown on BCB-covered SiO$_2$/Si substrates (Fig. 7) using the DPC method on the same substrate. The pinners dictated the locations of the droplets of $C_{60}$ and TIPS-pentacene solutions and, thus, the aligned crystals. In order to avoid the inter-diffusion of the two molecules during crystallization, the BCB layer in-between were etched away to induce dewetting of the solutions (Fig. 7A, black region). The obtained crystals are well-aligned and separated with distinct areas of $C_{60}$ and TIPS-pentacene crystals (Fig. 7B, C). Inverters were constructed by depositing Au top-contact electrodes, with FET channel length (L) of 100 µm and width (W) of 1 mm. The FET mobility in the inverter configuration (in the best-performance inverter, $\mu_{electron} = 0.64$; $\mu_{hole} = 0.63$ without channel geometry correction) is slightly lower than that in the individual FETs. One possible reason for the lower value is the slight inter-diffusion between the two molecules. Clear inverting functionality was observed (Fig. 7E). We achieved a gain as high as 155, which is among the highest values reported for organic complimentary inverters (Fig. 7F).
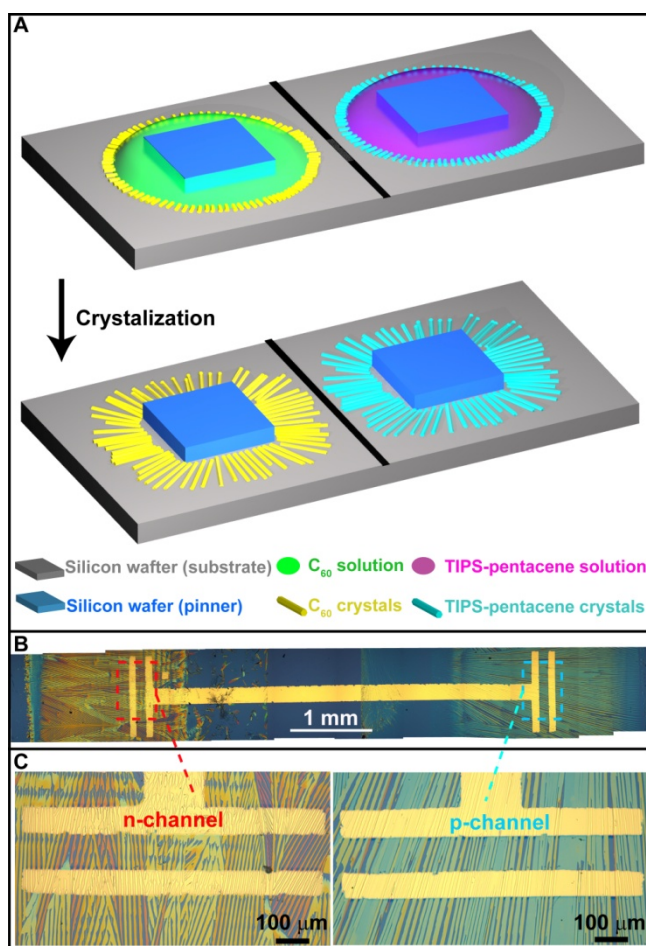
**Figure 7:** Schematic representations of patterning p- and n-type crystals on a common substrate using the DPC method. (A) One droplet of $C_{60}$ (n-channel, green) solution and the other droplet of TIPS-pentacene (p-channel, purple) solution are pinned by silicon wafers. In order to avoid the inter-diffusion of the two molecules, the black region between the two droplet is treated in advance by UV-ozone and becomes solvent-dewetting. As the solvent evaporates slowly, the crystals of $C_{60}$ and TIPS-pentacene nucleate near the contact lines of the droplets and, subsequently, grow along the receding direction (towards the centre) of the droplet, resulting in well-aligned crystals. (B) A composite image from several optical microscopy (OM) images, showing the positioned regions of well-aligned $C_{60}$ and TIPS-pentacene crystals. Au electrodes were deposited onto the crystals to define the p- and n-channel of the inverter. (C) Magnified images of (B) highlighting the channels.

## 5. Review and prospective on flexible and stretchable electronics.

We wrote an invited review for Accounts of Chemical Reviews related to flexible and stretchable electronics for electronic skin applications. Some proposed directions became part of the new AFOSR-funded program in the new contract. Here is a short summary of the review:

Skin is the body's largest organ, and is responsible for the transduction of a vast amount of information. This conformable material simultaneously collects signals from external stimuli that translate into information such as pressure, pain, and temperature. The development of an electronic material, inspired by the complexity of this organ is a tremendous, unrealized engineering challenge. However, the advent of carbon-based electronics may offer a potential solution to this longstanding problem. In this Account, we describe the use of an organic field-effect transistor (OFET) architecture to transduce mechanical and chemical stimuli into electrical signals. In developing this mimic of human skin, we thought of the sensory elements of the OFET as analogous to the various layers and constituents of skin. In this fashion, each layer of the OFET can be optimized to carry out a specific recognition function. The separation of multi-modal sensing among the components of the OFET may be considered a "divide and conquer" approach, where the electronic skin (e-skin) can take advantage of the optimized chemistry and materials properties of each layer.

This design of a novel micro-structured gate dielectric has led to unprecedented sensitivity for tactile pressure events. Typically, pressure sensitive components within electronic configurations have suffered from a lack of sensitivity or long mechanical relaxation times often associated with elastomeric materials. Within our

method, these components are direct compatible with OFETs and have achieved the highest reported sensitivity to date. Moreover, the tactile sensors operate on the timescale comparable with human skin, making them ideal candidates for integration as synthetic skin devices. The methodology is compatible with large-scale fabrication and employs simple, commercially available elastomers.

The design of materials within the semiconductor layer has led to the incorporation of selectivity and sensitivity within gas sensing devices and has enabled stable sensor operation within aqueous media. Furthermore, careful tuning of the chemical composition of the dielectric layer has provided a means to operate the sensor in real time within an aqueous environment without the need for encapsulation layers.

The integration of such devices as electronic mimics of skin will require the incorporation of biocompatible or biodegradable components. Toward this goal, OFETs may be fabricated with >99% biodegradable components by weight, and the devices are robust and stable, even in aqueous environments. Collectively, progress to date suggests that OFETs may be integrated within a single substrate to function as an electronic mimic of human skin, which could enable a large range of sensing-related applications from novel prosthetics to robotic surgery.
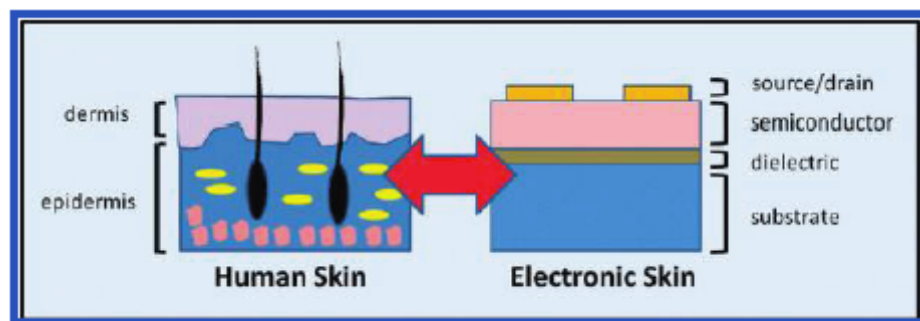


**Publications during reporting period**

1. G. Giri, E. Verploegen, S. Mannsfeld, S. Atahan-Evrenk, D. H. Kim, S. Y. Lee, H. A. Becerril, A. Aspuru-Guzik, M. F. Toney, Z. Bao, "Tuning charge transport in solution-sheared organic semiconductors using lattice strain", **Nature**, 480, 504-508, 2011.

2. A.N. Sokolov, S. Atahan-Evrenk, R. Mondal, H. B. Akkerman, R. S. Sanchéz-Carrera, S. Granados-Focil, J. Schrier, S. C. B. Mannsfeld, A. P. Zoombelt, Z. Bao, and A. Aspuru-Guzik, "From in silico computational discovery to experimental characterization of a high hole mobility organic crystal" **Nature Communication**, 2:437. DOI: 10.1038/ncomms1451, 2011.

3. P. Wei, T. Menke, B.D. Naab, K. Leo, M. Riede, and Z. Bao, "2-(2-Methoxyphenyl)-1,3-dimethyl-1H-benzoimidazol-3-ium Iodide as a New Air-Stable n-Type Dopant for Vacuum-Processed Organic Semiconductor Thin Films" **J. Am. Chem. Soc.** 134, pg 3999-4002, 2012.

4. Y. Jiang, J. Mei, A. L. Ayzner, M. F. Toney and Z. Bao,"5,11-Conjugation-extended low-bandgap anthradithiophene-containing polymer exhibiting enhanced thin-film order and field-effect mobility" **Chem Comm.**, 48, 7286-7288, 2012.

5. Y. Jiang , S. Hong , J.H. Oh , R. Mondal , T. Okamoto , E. Verploegen , M. F. Toney, M.D. McGehee and Z. Bao, "Impact of regioregularity on thin-film transistor and photovoltaic cell performances of pentacene-containing polymers" **J. Mater. Chem.**, 22, 4356-4363, 2012

6. T. Okamoto, Y. Jiang, H. A. Becerril, S. Hong, M. L. Senatore, M. L. Tang, M. F. Toney, T. Siegrist and Z. Bao. "Synthesis of regioregular pentacene-containing conjugated polymers" **J. Mater. Chem.,** 21, 7078-7081, 2011.

7. (Invited Review) M.L. Tang and Z. Bao. "Halogenated Materials as Organic Semiconductors", **Chem. Mater**., 23, 446-455, 2011.

8. Y. Chung, E. Verploegen, A. Vailionis, Y. Sun, Y. Nishi, B. Murmann and Z. Bao, "Controlling Electric Dipoles in Nanodielectrics and Its Applications forEnabling Air-Stable n-Channel Organic Transistors", **Nano Letters**, 11, 1161-1165, 2011.

9. H. Li, B. C.-K. Tee, J.J. Cha, Y. Cui, J.W. Chung, S.Y. Lee, and Z. Bao, "High-Mobility Field-Effect Transistors from Large-Area Solution-Grown Aligned C60 Single-Crystals", **J. Am. Chem. Soc.**, 134, pg 2760-2765, 2012.

10. H. Li, B. C.-K. Tee, J.W. Chung, S.Y. Lee, and Z. Bao, "High-Performance Transistors and Complementary Inverters Based on Solution-Grown Aligned Organic Single-Crystals", **Adv Mater.**, 24, 2588-2591, 2012.

11. Peng Wei, Joon Hak Oh, Guifang Dong and Zhenan Bao, "A 1H-Benzoimidazole Derivative as an n-Type Dopant and Its Use to Enable Air-Stable Solution-Processed n-Channel Organic Thin-Film Transistors." *J. Am. Chem. Soc.*, 132, 8852-8853, 2010.

12. Joon Hak Oh, Peng Wei, and Zhenan Bao, "Molecular n-type doping for air-stable electron transport in vacuum-processed n-channel organic transistors." **Appl. Phys. Lett.**, 97, 243305, 2010.

13. Ying Jiang, Toshihiro Okamoto, Hector A. Becerril, Sanghyun Hong, Ming Lee Tang, Alex C. Mayer, Jack E. Parmer, Michael D. McGehee and Zhenan Bao, "Anthradithiophene-Containing Copolymers for Thin-Film Transistors and Photovoltaic Cells", **Macromolecules**, 43, 6361–6367, 2010.

14. Toshihiro Okamoto, Colin Reese, Michelle L. Senatore, Ming L. Tang, Ying Jiang, Sean R. Parkin, Zhenan Bao, "2,9-Dibromopentacene: Synthesis and the role of substituent and symmetry on solid-state order", **Synthetic Metals**, 160 , 2447-2451, 2010.

**Patents filed:**

Stanford Docket# 10-054
Invention Title:  Air stable n-channel organic thin-film transistors by
n-type doping
Disclosed to Sponsor:  3/2/10
Inventors:  Zhenan Bao, Joon Hak Oh, & Peng Wei
Patent Activity:  Utility Application 13/079,879 filed 4/5/11; sent to
sponsor 5/4/11

Stanford Docket# 10-055
Invention Title:  n-Type Dopants for Organic Electronics
Disclosed to Sponsor:  3/2/10
Inventors:  Zhenan Bao & Peng Wei
Patent Activity:  Utility Application 13/080,564 filed 4/5/11; sent to
sponsor 4/13/11

Stanford Docket# 10-055A
Invention Title:  n-Type Dopants for Organic Electronics
Disclosed to Sponsor: 5/10/12
Inventors:  Zhenan Bao, Benjamim Naab, & Peng Wei
Patent Activity:  Utility Application 13/440,714 filed 4/5/12; sent to
sponsor 5/10/12